Adaptive Probabilistic Constellation Shaping based on Enumerative Sphere Shaping for FSO Channel with Turbulence and Pointing Errors

Jingtian LIU⁽¹⁾, Xiongwei YANG⁽¹⁾, Yi WEI⁽¹⁾, Jianjun YU⁽²⁾, Feng ZHAO⁽¹⁾

Abstract—Free-space optical (FSO) transmission enables fast, secure, and efficient next-generation communications with abundant spectrum resources. However, atmospheric turbulence, pointing errors, path loss, and atmospheric loss induce random attenuation, challenging link reliability. Adaptive rate control technology enhances spectrum utilization and reliability. We propose an adaptive probabilistic constellation shaping (A-PCS) coherent system utilizing enumerated spherical shaping (ESS) for distribution matching. With PCS-64QAM, the system achieves continuous rate control from conventional QPSK-equivalent to 64QAM spectral efficiency, providing quasi-continuous control with granularities of approximately 0.05 bits/4D for spectral efficiency and 0.1 dB for the post-FEC SNR threshold, and a maximum control depth of 12.5 dB. Leveraging ESS for efficient sequence utilization, it offers higher spectral utilization and finer control granularity than constant composition DM (CCDM)-based A-PCS systems. We further model and analyze the FSO channel, presenting calculations and comparisons of outage probability and ergodic capacity under varying turbulence intensities and pointing errors. Results demonstrate 99.999 % reliability at maximum $\sigma_{\rm R}^2=1.39$ and $\sigma_{\rm s}=0.5$ m, meeting requirements under severe turbulence and large pointing errors.

Index Terms—Free-space optical transmission, adaptive Probabilistic Constellation Shaping, atmospheric turbulence, pointing errors, channel modeling, reliability enhancement.

I. INTRODUCTION

The rapid advancement of global digitalization has accelerated the development of sixth-generation (6G) mobile communication systems. In addition to achieving comprehensive terrestrial coverage, 6G requires the establishment of a robust integrated communication network spanning air, space, and sea domains [1]–[3]. In free-space wireless communications, microwave-based systems offer a mature and reliable solution; however, their limited spectral resources in the GHz band constrain high-capacity data transmission, failing to meet the escalating demand for bandwidth in next-generation networks. In contrast, free-space optical (FSO) communication leverages abundant spectrum resources at higher frequencies, offering significant advantages such as broad bandwidth, long transmission distance, and enhanced security [4], [5]. Moreover, FSO systems can interface seamlessly with existing fiber-optic

 $E{\text{-}mail\ of\ corresponding\ author:\ jingtian.liu@xupt.edu.cn,\ hfengzhao@xupt.edu.cn}}$ xupt.edu.cn

infrastructures, supporting both line-of-sight and non-line-of-sight transmission modes.

Nevertheless, FSO signal propagation through the atmosphere is susceptible to various channel impairments. Variations in temperature and pressure along the transmission path induce refractive index inhomogeneities, leading to atmospheric turbulence. When combined with pointing errors caused by random vibrations at transceivers, these effects result in random fading of the received signal power [6]. Adverse weather conditions-such as fog, haze, and snowfurther attenuate the optical signal through photon absorption, causing severe degradation [7]. Such channel characteristics pose substantial challenges to the reliability of FSO links.

To enhance link reliability, adaptive transmission schemes have been proposed, wherein modulation formats or errorcorrecting codes are dynamically selected according to channel conditions. For instance, [8] introduced an adaptive strategy based on received signal-to-noise ratio (SNR), switching among five modulation schemes from OOK to 32PAM according to predefined SNR thresholds. When channel conditions deteriorate beyond the capability of OOK, the system switches to an RF link employing modulations from BPSK to 32QAM. By accounting for atmospheric turbulence in FSO and multipath effects in RF, the authors demonstrated significant gains in spectral efficiency and outage performance. Similarly, [9] incorporated low-density parity-check (LDPC) codes with code rates ranging from $\frac{1}{4}$ to $\frac{9}{10}$ and modulation orders from QPSK to 32APSK, achieving 28 adaptive switching levels. Combined with deep learning-based channel prediction, this approach further improved spectral efficiency and resilience against deep fading.

Although increasing the number of modulation levels improves granularity and spectral utilization, the inherent spectral efficiency gap between discrete modulation formats limits the minimum step size to approximately 0.4 bits/4D. To overcome this limitation, adaptive probabilistic constellation shaping (A-PCS) has been introduced. By adjusting the probability of constellation points according to a Maxwell–Boltzmann (MB) distribution [10], PCS enables near-continuous tuning of spectral efficiency, approaching the Shannon capacity limit. In [11], an intensity modulation-based A-PCS scheme was demonstrated, combining PCS-M-PAM with multi-rate LDPC codes to achieve fine-grained rate adaptation and improve ergodic capacity. With advances in high-order quadrature amplitude modulation (QAM) and coherent detection, [12] and [13] proposed A-PCS systems using CCDM and QAM

⁽¹⁾ School of Electronic Engineering, Xi'an University of Posts and Telecommunications, Xi'an, 710121, China; ⁽²⁾ School of Information Science and Technology, Fudan University, Shanghai, 200433, China.

constellations. By integrating a time-window averaging algorithm for channel state prediction and incorporating control redundancy, their experiments demonstrated high transmission reliability and considerable gains in overall throughput.

Despite these advances, several challenges remain in A-PCS design. First, existing studies often assume infinite block lengths for CCDM, overlooking practical complexity and rate loss due to finite block length constraints. Second, many works do not fully incorporate FSO channel effects-such as atmospheric turbulence and pointing errors-into the performance analysis of A-PCS systems, leaving a gap in the modeling of outage probability and ergodic capacity. In this paper, we propose a novel A-PCS framework that considers implementation complexity and employs a finite-length distribution matcher. By leveraging the low rate loss of ESS at short block lengths, our system achieves finer adaptation granularity and higher spectral efficiency. Furthermore, we develop a comprehensive channel model for FSO links and derive analytical expressions for outage probability and ergodic capacity under various turbulence strengths and misalignment conditions. Through comparative analysis, we demonstrate the superior adaptability and high reliability of the proposed A-PCS system.

The remainder of this paper is organized as follows: Section II introduces PCSs principles and channel modeling; Section III presents the system architecture and modeling of the proposed A-PCS scheme; Section IV evaluates the system performance under various channel conditions; and Section V summarizes the key findings and conclusions.

II. SYSTEM DESCRIPTION AND DEFINITIONS

A. Channel Model

We consider a FSO communication system that employs coherent detection with either conventional or probabilistically shaped M-ary quadrature amplitude modulation (M-QAM). The input bit sequence, denoted as $\mathbf{B}^k = \{B_1, \dots, B_k\}$, comprises independent and identically distributed bits following a Bernoulli distribution with parameter 1/2. If the target symbol sequence is uniformly distributed, a binary reflected Gray code (BRGC) maps the bits directly to an M-QAM symbol sequence $\mathbf{S}^n = \{S_1, \dots, S_n\}$, where $n = k/\log_2 M$. A forward error correction (FEC) code with rate $R_{\rm C}$ is incorporated to ensure reliable transmission. Otherwise, PCS is applied: a distribution matcher (DM) generates a non-uniformly distributed symbol sequence using a binary labeling strategy, which integrates FEC coding. Further details on PCS are provided in Section II-B. The symbol sequence is subsequently filtered to produce an electrical signal, which modulates the optical source. After propagation through the channel, the optical beam is collected by a lens at the receiver and coherently mixed with a local oscillator for heterodyne detection, enabling coherent reception. In our simulations, laser phase noise and frequency offset are neglected, under the assumption that these impairments can be perfectly compensated via digital signal processing. Following filtering, the signal is down-sampled (due to the absence of phase noise). Finally, the electrical signal-to-noise ratio (SNR_{elec}) is measured from the equalized constellations, and the generalized mutual information (GMI) is computed.

The FSO channel is subject to four primary impairments: atmospheric turbulence $h_{\rm a}$, atmospheric loss $h_{\rm l}$, pointing errors $h_{\rm p}$ [6], and geometric spread. For short-range links, geometric spread is integrated into the pointing errors component as a geometric expansion term. These impairments, combined with ambient light noise and thermal noise-modeled accurately as additive white Gaussian noise (AWGN) [14]-directly degrade the SNR at the receiver. Based on the above effects, the received signal is conventionally modeled as [15]:

$$y = (h\kappa P_{\rm x})^{\tau/2}x + n$$
, where $h = h_{\rm l}h_{\rm p}h_{\rm a}$. (1)

Here, x represents the transmitted signal, τ is a detector-specific parameter ($\tau=1$ for heterodyne detection and $\tau=2$ for direct detection), $h_{\rm l}$ denotes the atmospheric loss (modeled via the Beer-Lambert law and assumed constant), $h_{\rm p}$ and $h_{\rm a}$ are random variables following Gamma-Gamma and Rayleigh distributions, respectively (as detailed below), κ is the receiver's optical-to-electrical conversion efficiency, and n is AWGN with variance $\sigma_{\rm n}^2$. The corresponding instantaneous SNR is given by:

$$\gamma_{\rm FSO}(h) = \frac{(h\kappa P_{\rm x})^{\tau}}{\sigma_{\rm p}^2},$$
 (2)

where h is a random variable whose distribution is specified in Eq. 10.

1) Atmospheric loss: The atmospheric attenuation coefficient characterizes the total loss due to absorption and scattering by atmospheric molecules and aerosols. At a wavelength of 1550 nm, molecular absorption is negligible, with an approximate value of 0.01 dB/km. The dominant factor in atmospheric attenuation is particle scattering, which encompasses molecular scattering, aerosol scattering, and scattering by hydrometeors such as haze, fog, snow, rain, and hail. This attenuation can be modeled using the exponential Beer-Lambert law as [7]:

$$h_1(\lambda, z) = \exp(-\sigma(\lambda)z),$$
 (3)

where $\sigma(\lambda)$ is the wavelength-dependent attenuation coefficient, which is a function of wavelength and the meteorological visibility range V. The meteorological visibility range is defined as the distance at which the transmittance at 550 nm falls to a threshold of $\epsilon = 0.05$ [7]. (Note: Increased fog concentration is positively correlated with reduced turbulence intensity [16].)

2) Atmospheric turbulence: Atmospheric turbulence arises from temperature and pressure gradients that induce refractive index inhomogeneities. These inhomogeneities form turbulent eddies that scatter optical beams based on the ratio of eddy size to beam width. When the eddy size is comparable to the beam width, focusing and defocusing effects cause random irradiance fluctuations at the receiver, known as scintillation. Scintillation, manifested as intensity fluctuations, is the dominant fading effect in FSO channels, degrading the SNR through deep fades [17]. Several statistical models describe scintillation-induced fading: the log-normal distribution for weak-to-moderate turbulence [18], the double Weibull distribution for moderate-to-strong turbulence [19],

the K-distribution for strong turbulence [20], and the Gamma-Gamma (GG) distribution for weak-to-strong turbulence [21]. Since our analysis covers a wide range of turbulence conditions from weak to strong, we employ the GG distribution, which agrees well with experimental measurements and models the fading as the product of large-scale and small-scale eddy effects. The probability density function (PDF) of the GG distribution for the intensity $h_{\rm a}$ is given by [21]:

$$f(h_{\rm a}) = \frac{2(\alpha\beta)^{\frac{\alpha+\beta}{2}} h_{\rm a}^{\frac{\alpha+\beta}{2}-1}}{\Gamma(\alpha)\Gamma(\beta)} K_{\alpha-\beta} \left(2\sqrt{\alpha\beta h_{\rm a}}\right), h_{\rm a} > 0 \quad (4)$$

where $K_a(\cdot)$ is the modified Bessel function of the second kind of order a, $\Gamma(\cdot)$ is the gamma function, and α and β represent the effective numbers of small-scale and large-scale eddies, respectively. These parameters are defined as:

$$\alpha = \left[\exp\left(\frac{0.49\chi^2}{(1 + 0.18d^2 + 0.5\chi^{12/5})^{7/6}}\right) - 1 \right]^{-1}, \quad (5)$$

$$\beta = \left[\exp\left(\frac{0.51\chi^2 (1 + 0.69\chi^{12/5})^{-5/6}}{(1 + 0.9d^2 + 0.62d^2\chi^{12/5})^{7/6}} \right) - 1 \right]^{-1}, \quad (6)$$

where $\chi^2=0.5C_n^2k^{7/6}z^{11/6}$ and $d=\sqrt{ka^2/(4z)}$. Here, $k=2\pi/\lambda$ is the optical wave number, a is the diameter of the receiver aperture, z is the link range in meters, and C_n^2 is the refractive index structure parameter, which depends on temperature, pressure, and humidity. The turbulence severity is determined by the refractive index structure parameter, wave number, and link range, often quantified by the Rytov variance, $\sigma_{\rm R}^2$ [22]:

$$\sigma_{\rm R}^2 = 1.23C_n^2 k^{7/6} z^{11/6} = 2.46\chi^2. \tag{7}$$

Thus, in our simulations, the turbulence strength is varied through $\sigma_{\rm R}^2$, and $h_{\rm a}=1$ under turbulence-free conditions. The fading process in atmospheric turbulence channels has a coherence time on the order of 10^{-3} to 10^{-2} seconds, which is much longer than typical symbol durations (around 10^{-9} seconds) [23], [24]. Therefore, the channel gain $h_{\rm a}$ remains approximately constant during each transmission. This slow fading makes interleaving techniques ineffective for averaging over fading states. Consequently, such channels exhibit blockfading characteristics (also known as slow-fading or nonergodic channels) and can be modeled using exponentially correlated processes via first-order stochastic differential equations [25].

3) Pointing Errors: In line-of-sight FSO communication links, the light beam propagating through the atmosphere undergoes geometric expansion, leading to a continuous increase in beam width. Since the received beam width typically exceeds the size of the receiving aperture, only a portion of the transmitted energy is captured, resulting in deterministic geometric expansion loss. This loss is minimized when the beam center aligns perfectly with the receiving aperture. However, random factors such as building vibrations induced by wind loads or thermal expansion can cause transmit beam jitter [26], leading to misalignment between the received beam and the photodiode aperture. This misalignment prevents the beam focus from coinciding with the aperture focal point, degrading pointing accuracy and further attenuating the received signal

strength. The fixed geometric spread is correlated with random pointing accuracy: a larger received beam width reduces the attenuation depth due to pointing errors but increases the geometric spread loss. These effects are commonly modeled jointly. For a Gaussian beam, the pointing errors loss $h_{\rm p}$ due to misalignment can be expressed in Gaussian form as:

$$h_{\rm p}(r;z) \approx A_0 \exp\left(-\frac{2r^2}{w_{z_{\rm eq}}^2}\right),$$
 (8)

where r denotes the pointing error, defined as the radial distance between the center of the beam footprint and the center of the detector. By assuming that the elevation and horizontal sway displacements follow independent and identical Gaussian distributions [6], the PDF of $h_{\rm p}$ can be derived as:

$$f_{h_{\mathbf{p}}}(h_{\mathbf{p}}) = \frac{\gamma^2}{A_0^{\gamma^2}} h_{\mathbf{p}}^{\gamma^2 - 1}, \quad 0 \le h_{\mathbf{p}} \le A_0,$$
 (9)

where $\gamma=w_{z_{\rm eq}}/(2\sigma_{\rm s})$ represents the ratio of the equivalent beam radius $w_{z_{\rm eq}}$ at the receiver to the standard deviation of the pointing error displacement (jitter) $\sigma_{\rm s}$. The parameter A_0 corresponds to the fraction of collected power when the beam center coincides with the receiving aperture, accounting for inherent beam spreading effects. Thus, $h_{\rm p}=A_0$ in the absence of pointing error.

4) Composite Channel Model: Given the PDFs of the atmospheric turbulence gain h_a and the pointing errors gain h_p , as provided in Eq. 4 and Eq. 9, respectively, the PDF of the composite channel gain coefficient $h = h_1 h_p h_a$ can be expressed as [6]:

$$f_{h}(h) = \frac{2\gamma^{2}(\alpha\beta)^{\frac{\alpha+\beta}{2}}}{(A_{0}h_{1})^{\gamma^{2}}\Gamma(\alpha)\Gamma(\beta)}h^{\gamma^{2}-1} \times \int_{\frac{h}{A_{0}h_{1}}}^{\infty} h_{a}^{\frac{\alpha+\beta}{2}-1-\gamma^{2}} K_{\alpha-\beta} \left(2\sqrt{\alpha\beta h_{a}}\right) dh_{a}.$$
(10)

where the integration can be evaluated using numerical techniques.

B. Probabilistic Constellation Shaping with Enumerative Sphere Shaping

PCS aims to generate symbol sequences that adhere to a target probability distribution. As established in [10], the MB distribution is the optimal symbol probability distribution for the AWGN channel under a fixed average energy constraint. A key component in achieving this distribution is the DM, which transforms uniformly distributed input symbol sequences into sequences conforming to the target distribution. These sequences emulate discrete memoryless sources and are designed to be invertible, ensuring accurate recovery of the original input symbols via a dematching process.

Let the input sequence consist of k independent and identically distributed bits, denoted as $\mathbf{B}^{\mathbf{k}} = \{B_1, \dots, B_k\}$, each following a Bernoulli distribution with probability $\frac{1}{2}$. In the fixed-to-fixed DM process, a bijective mapping function f maps $\mathbf{B}^{\mathbf{k}}$ to a length-N sequence $\tilde{\mathbf{A}}^{\mathbf{N}} = f(\mathbf{B}^{\mathbf{k}})$, where

$$P_A(a) = \begin{cases} K(\lambda)e^{-\lambda a^2}, & \text{for } a \in A, \\ 0, & \text{otherwise,} \end{cases}$$
 (11)

where λ is the shaping parameter controlling the distribution's variance, and $K(\lambda)$ is a normalization constant.

This mapping is crucial in PCS for tailoring signal constellations to specific channel conditions, thereby improving system performance. The bijectivity of f guarantees reversibility through f^{-1} , ensuring reliable data recovery in optical communication systems.

CCDM, introduced by Schulte and Böcherer [27], generates sequences with a fixed symbol composition. However, CCDM suffers from significant rate loss at short block lengths and requires long sequences to achieve high shaping gains. In contrast, ESS [28], [29], proposed by Amari et al. and extended by Gültekin et al., maps input bits onto a high-dimensional sphere to optimize energy efficiency. ESS exhibits lower rate loss than CCDM at the same shaping rate. For a block length of 108, ESS achieves only one-fifth the rate loss of CCDM. This advantage stems from ESS utilizing all energy levels below a fixed maximum energy. As the block length increases, the performance of ESS and CCDM converges.

Sphere coding constrains sequences to an N-dimensional sphere. The induced one-dimensional distribution converges to the MB distribution as $N \to \infty$. ESS employs bounded-energy amplitude sequences (up to $E_{\rm max}$) and uses lexicographic indexing to enumerate sequences. Graphically, ESS can be represented by a bounded-energy trellis where states correspond to energy levels and branches represent amplitudes.

In this trellis, each sequence $\mathbf{a}^{\mathbf{N}} = (a_1, \dots, a_N)$ corresponds to a unique path of N branches. A branch from column n-1 to n represents the amplitude a_n . Nodes in column n indicate the cumulative energy up to dimension n:

$$E((a_1, \dots, a_n)) = \sum_{i=1}^n a_i^2.$$
 (12)

In Fig. 1, energy values are shown as black numerals. Paths start from the zero-energy node (bottom-left) and end at column N=4. The energy increments by 1 or 9 for $a_n=1$ or 3, respectively. Terminal nodes have energies in $\{N,N+8,N+16,\ldots,E_{\max}\}$ for $\mathcal{A}=\{1,3\}$. The energy at any node in column n is given by:

$$e = n + 8l, (13)$$

where $l \in [0, L-1]$ and L is the number of energy levels:

$$L = \left| \frac{E_{\text{max}} - N}{8} \right| + 1. \tag{14}$$

If the expression in Eq. 14 is an integer, $E_{\rm max}$ can be derived as:

$$E_{\text{max}} = 8(L - 1) + N. \tag{15}$$

Each node is identified by (n,e). Red numerals in the figure denote the number of paths to a node at n=N, computed recursively for $n=N-1,\ldots,0$ and $0\leq e\leq E_{\max}$ as:

$$T_n^e = \sum_{a \in A} T_{n+1}^{e+a^2},\tag{16}$$

with initial condition $T_N^e = 1$. Only states with $e \in [n, E_{\max} + n - N]$ are considered per column.

The trellis enables sequence enumeration. For example, from node (3,11), paths lead to (4,12) (amplitude 1) or (4,20) (amplitude 3), so $T_3^{11}=2$. From (1,1), $T_1^1=7$. The total sequences are $T_0^0=11$, encoding $k=\lfloor \log_2 T_0^0 \rfloor =3$ bits. For this example:

$$R_{\rm DM} = \frac{k}{N} = 0.75 \text{ bits/amplitude},$$
 (17)

$$P_A(1) = \frac{T_1^{a^2}}{\sum_{b \in A} T_1^{b^2}} = \frac{7}{11}, \qquad P_A(3) = \frac{4}{11},$$
 (18)

$$E_{\text{av}} = N \sum_{a \in \mathcal{A}} P_A(a) a^2 = 15.6364,$$
 (19)

$$R_{\text{loss}} = H(A_{\text{MB}}) - R_{\text{DM}} = 0.95 - 0.75 = 0.2 \text{ bits/amplitude.}$$
(20)

Here, $A_{\rm MB}$ denotes a random variable following the MB distribution with average energy $E_{\rm av}$. The rate loss formula in Eq. 20 applies to both ESS and CCDM. As $N\to\infty$, ESS achieves the MB distribution, and $R_{\rm loss}\to0$.

C. PCS Performance Assessment Metrics

To address the complexity inherent in coded modulation for optical communication systems, Bit-Interleaved Coded Modulation (BICM) is widely adopted as an efficient approach. BICM separates the coding and mapping processes, facilitating a more flexible and practical system design. In BICM systems, forward error correction (FEC) coded bits undergo interleaving, which disperses potential burst errors during transmission, thereby enhancing the robustness of the communication link.

After interleaving, the bits are grouped into blocks and mapped onto modulation symbols for transmission over the optical channel. At the receiver, the system demodulates these symbols to recover the original information. To support this, soft information-typically in the form of bit-wise a posteriori probabilities or log-likelihood ratios-is extracted from the demodulated symbols and passed to the decoder. This procedure is referred to as Bit-Metric Decoding (BMD).

BMD is particularly effective in channels with non-uniform error characteristics, as it provides a reliability measure for each bit based on the received symbol. The flexibility of BICM, combined with the efficiency of BMD, makes it an attractive coding scheme for modern optical communication systems, offering a balance between performance and complexity.

BICM can be modeled as m parallel, memoryless, and independent binary channels, where $m = \log_2(M)$ for an M-symbol constellation. The maximum achievable information rate of BICM is known as the generalized mutual information (GMI), defined as [30], [31]:

$$GMI_{BMD}(\gamma_{FSO}) \approx H(X) - \frac{1}{N} \sum_{k=1}^{N} \sum_{i=1}^{m} \log_2 \frac{\sum_{x \in A} q_{Y|X}(y_k|x) p_X(x)}{\sum_{x \in A_{b_k,i}} q_{Y|X}(y_k|x) p_X(x)},$$
(21)

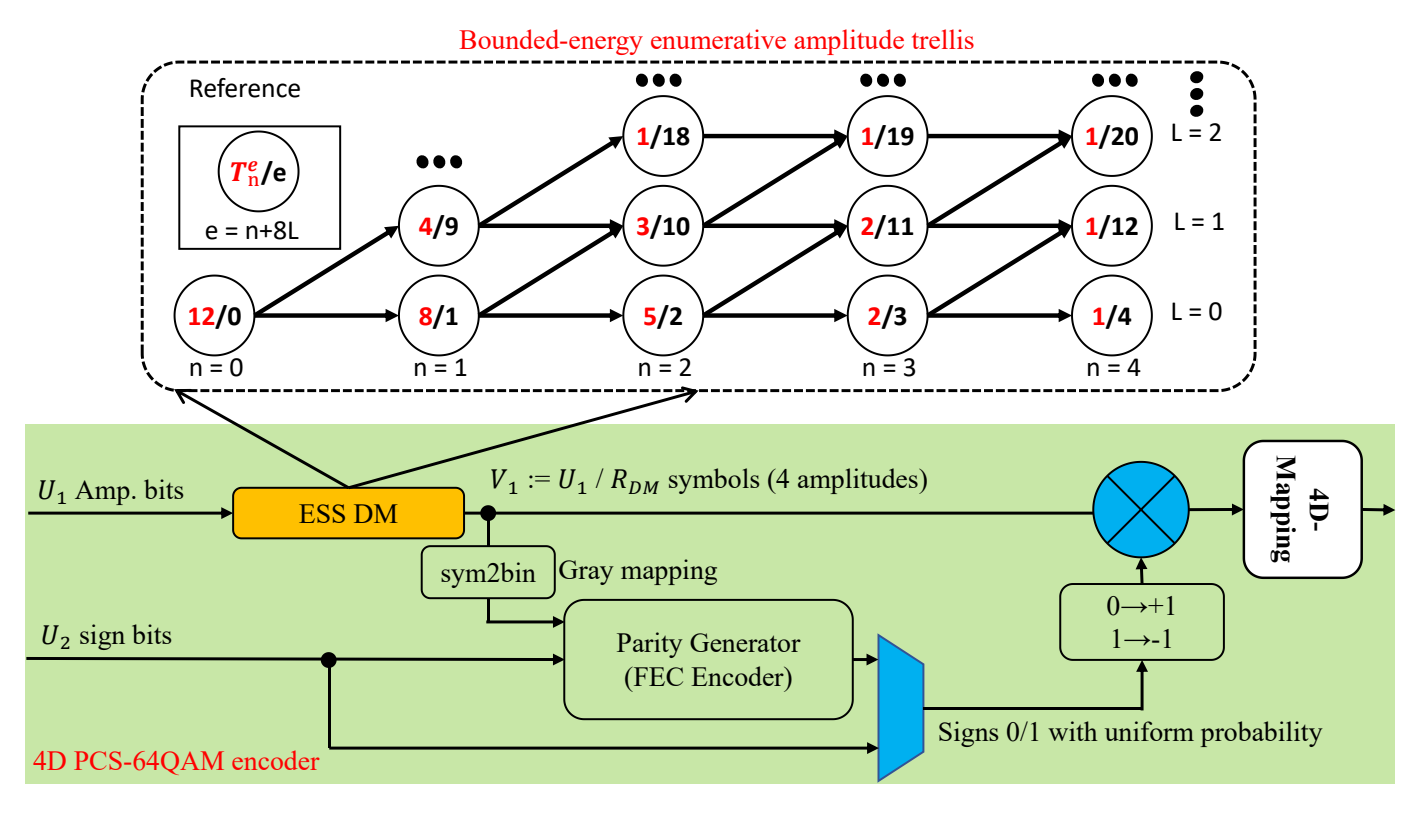


Fig. 1. Block diagram of 4D PCS-64QAM encoder with FEC and ESS distribution matcher. An example of bounded-energy enumerative amplitude trellis for $\mathcal{A} = \{1,3\}$, N=4, and $E_{\max}=20$, is shown in the upper image, which can achieve A-PCS encoding at arbitrary spectral efficiency by changing the energy boundary through setting the value of L.

Here, $q_{Y|X}$ denotes the auxiliary channel conditional probability, y_k represents the k-th received symbol out of N symbols in an AWGN channel with signal-to-noise ratio $\gamma_{\rm FSO}$, and $A_{b_{k,i}}$ is the set of 4D constellation symbols whose i-th bit equals $b_{k,i} \in \{0,1\}$. The final term, corresponding to channel loss, can be estimated via Monte Carlo methods. Although BICM incurs a capacity loss compared to coded modulation-constrained capacity, employing Gray mapping minimizes this loss, making it acceptable for practical applications.

Furthermore, in PCS, DM is used to optimize the transmitted symbol distribution, thereby improving system efficiency and performance. Considering finite-length DM is crucial, as practical implementations involve constrained DM lengths. Conventionally, GMI is estimated under the assumption of infinite-length DM, where rate loss is negligible. However, in real-world scenarios, finite DM length introduces a non-negligible rate loss that must be accounted for.

The GMI computation for finite-length one-dimensional DM involves evaluating the information content per amplitude shift keying (ASK) symbol for both infinite and finite DM lengths. This requires incorporating the rate loss due to finite DM into the GMI estimation, enabling a more accurate assessment of system performance. Thus, the GMI for finite-length DM in 4D M-QAM is defined as:

$$GMI_{4D}(\gamma_{FSO}) = GMI_{BMD}(\gamma_{FSO}) - 4R_{loss}.$$
 (22)

where $R_{\rm loss}$ is introduced in Eq. (20), with detailed derivations provided in the appendix of [32]. The factor of 4 accounts for the four dimensions in 4D M-QAM ((two pairs of I and Q

signals in two polarizations). Eq. (22) is used in subsequent sections to compare GMI across DMs with varying rate losses.

III. THE PROPOSED A-PCS DESIGN WITH ESS

This study investigates an A-PCS FSO communication system that utilizes a four-dimensional (4D) PCS-64QAM encoder at the transmitter, as illustrated in Fig. 2. The system employs ESS distribution matching (DM) with a block length of n=108, selected to balance complexity and rate loss. Additionally, it incorporates a LDPC code (length = 64,800 bits, code rate $R_{\rm C}=\frac{5}{6}$) compliant with the DVB-S2 standard.

A. Implementation of A-PCS

As depicted in Fig. 1, the input bit stream is partitioned into two components: U_1 amplitude bits and U_2 sign bits. The amplitude bits U_1 are fed into the ESS DM, which encodes them into amplitude symbols $V_1 = \frac{U_1}{R_{\mathrm{DM}}}$ for M-QAM modulation. For 64QAM, the amplitude levels are 1, 3, 5, and 7. Here, $R_{\rm DM}$ denotes the distribution matcher rate, determined by the ESS shaping parameter L. Subsequently, for each symbol, a 2-bit pattern is assigned via Gray mapping. These Gray-mapped bits, along with the uniformly distributed sign bits U_2 , are input to the forward error correction (FEC) encoder operating at a rate of $R_{\rm C} = \frac{k}{n}$. The redundant parity bits (n-k) from the FEC encoder are multiplexed with U_2 to form the symbol signs based on the $(-1)^p$ mapping (i.e., $0 \mapsto +1$ and $1 \mapsto -1$). Finally, the symbols are mapped to dual-polarization 4D 64QAM for transmission. The total net bit rate of the 4D PCS-M-QAM system is given by:

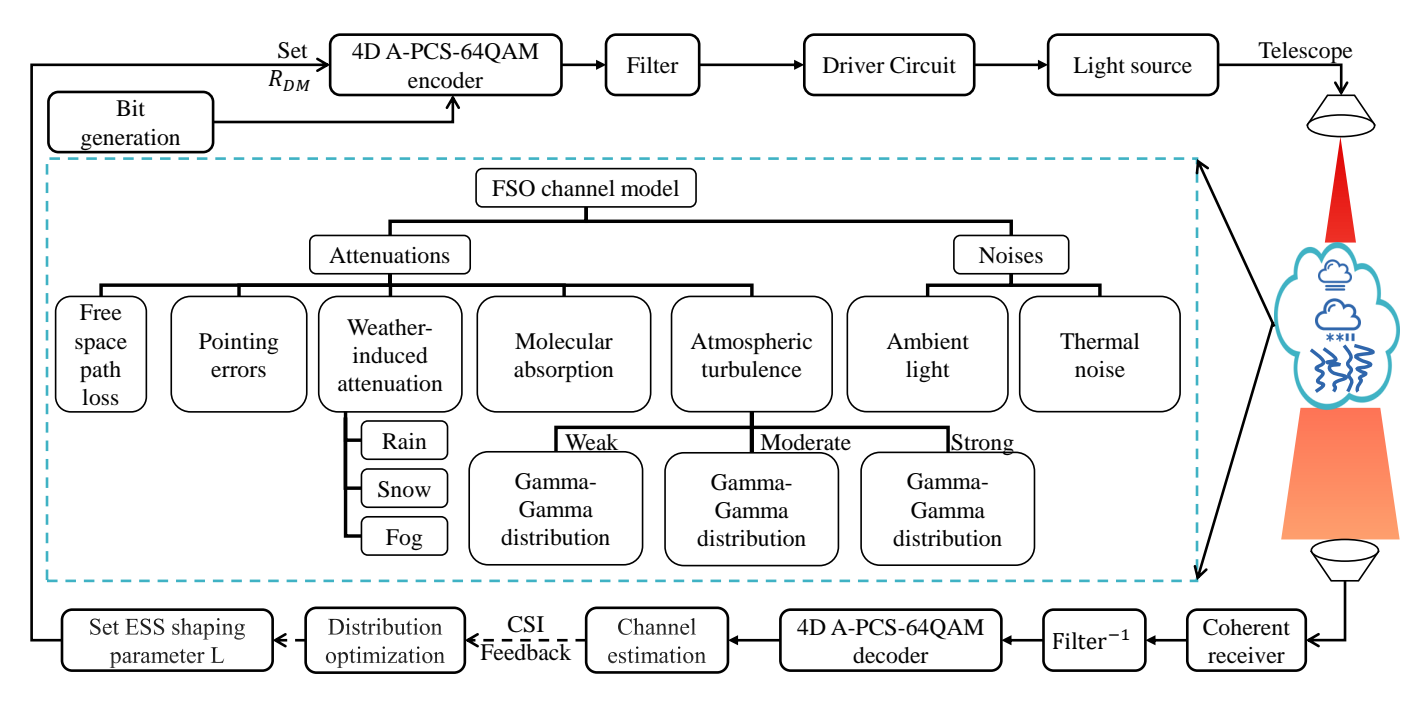


Fig. 2. Block diagram of adaptive 4D PCS-64QAM transmitter architecture with FEC and ideal CSI feedback. The channel effects are shown in the middle.

$$R_{\text{tot-4D}} = 4 + 4R_{\text{DM}} - 2m(1 - R_{\text{C}}),$$
 (23)

where $0 < R_{\rm DM} \leq \frac{m-2}{2}$ and $\frac{m-2}{m} \leq R_{\rm C} < 1$. The minimum value of $R_{\rm DM}$ corresponds to the DM outputting a single amplitude level, equivalent to 4D QPSK. The maximum value of $R_{\rm DM}$ indicates no shaping is applied, resulting in conventional 4D M-QAM. The minimum value of $R_{\rm C}$ occurs when $U_2=0$, meaning all required sign bits can be generated solely from FEC encoding of the DM output; a lower FEC rate would produce redundant bits that cannot be accommodated. For 64QAM (m=6), the total rate simplifies to $R_{\rm tot-4D}=4R_{\rm DM}+12R_{\rm C}-8$, with $0 < R_{\rm DM} \leq 2$ and $\frac{2}{3} \leq R_{\rm C} < 1$.

As shown in Fig. 2, assuming perfect prediction and feedback of channel state information (CSI) to the transmitter enables dynamic optimization of the signal probability distribution. When channel conditions improve or deteriorate, the shaping coefficient L can be adjusted-increased or decreasedto modify the distribution matching rate $R_{\rm DM}$ and subsequently the total net bit rate $R_{\text{tot-4D}}$, in accordance with Eqs. (12)–(16) and Eq. 23. This adjustment exhibits a positive correlation: as L varies, $R_{\text{tot-4D}}$ increases or decreases, leading to a corresponding change in the SNR threshold $\gamma_{\rm thr}$ required for error-free transmission at a fixed FEC rate. The threshold adapts until it lies just below the received SNR, thereby achieving error-free transmission and maximizing channel capacity utilization. In practice, Fig. 3 can be employed to construct a lookup table for setting L based on the target net bit rate. For any given $R_{\text{tot-4D}}$, a unique post-FEC error-free transmission SNR threshold $\gamma_{\rm thr}$ can be determined, since the instantaneous capacity GMI_{4D} is monotonically increasing with SNR (as detailed in Sec. II.A of [6]):

$$\gamma_{\rm thr} = \text{GMI}_{4D}^{-1}(R_{\rm tot-4D}). \tag{24}$$

By flexibly adjusting $R_{\rm tot\text{-}4D}$, a control range $\gamma_{\rm R}$ for the SNR threshold can be established to accommodate instantaneous channel fading. This range is defined as:

$$\gamma_{\rm R} = \frac{\rm GMI_{4D}^{-1}(R_{\rm tot.4D}^{\rm max})}{\rm GMI_{4D}^{-1}(R_{\rm tot.4D}^{\rm min})} = \frac{\gamma_{\rm thr}^{\rm max}}{\gamma_{\rm thr}^{\rm min}},\tag{25}$$

where $\gamma_{\rm R}$ represents the maximum instantaneous attenuation range controllable by the A-PCS system. In our model, the channel gain follows the distribution given in Eq. 10. The ideal channel gain $h_{\rm ideal}$, in the absence of turbulence and pointing errors, is expressed as:

$$h_{\text{ideal}} = A_0 h_l, \tag{26}$$

where A_0 and h_l are deterministic parameters. Substituting Eq. 26 into Eq. 10, the instantaneous attenuation $A_{\rm inst}$ relative to the ideal case is derived as:

$$A_{\text{inst}}(h) = \frac{\gamma_{\text{FSO}}(h_{\text{ideal}})}{\gamma_{\text{FSO}}(h)} = \frac{A_0 h_l}{h}.$$
 (27)

When $A_{\rm inst} \leq \gamma_{\rm R}$, error-free transmission can be maintained through rate adaptation; thus, outage occurs only when $A_{\rm inst} > \gamma_{\rm R}$. Defining h_0 such that $A_{\rm inst}(h_0) = \gamma_{\rm R}$, we obtain $h_0 = \frac{A_0 h_1}{\gamma_{\rm R}}$. The outage probability $P_{\rm out}$ for given turbulence and pointing error severities, denoted by $[\sigma_R^2, \sigma_s]$, is then:

$$P_{\text{out}}(\sigma_R^2, \sigma_s, \gamma_R) = \int_0^{h_0} f_h(h) dh = \int_0^{\frac{A_0 h_l}{\gamma_R}} f_h(h) dh.$$
 (28)

For an A-PCS system, the maximum net bit rate $R_{\mathrm{tot-4D}}^{\mathrm{max}}$ is achieved when $h=h_{\mathrm{ideal}}$. Outage occurs when $A_{\mathrm{inst}}>\gamma_{\mathrm{R}}$, corresponding to $h<\frac{A_0h_l}{\gamma_{\mathrm{R}}}$. The instantaneous transmission rate R_{inst} is adaptively adjusted based on real-time attenuation. For channel gains in the range $\frac{A_0h_l}{\gamma_{\mathrm{R}}}\leq h\leq A_0h_l$, R_{inst} is set to ensure $\gamma_{\mathrm{thr}}\leq\gamma_{\mathrm{FSO}}$, guaranteeing error-free transmission.

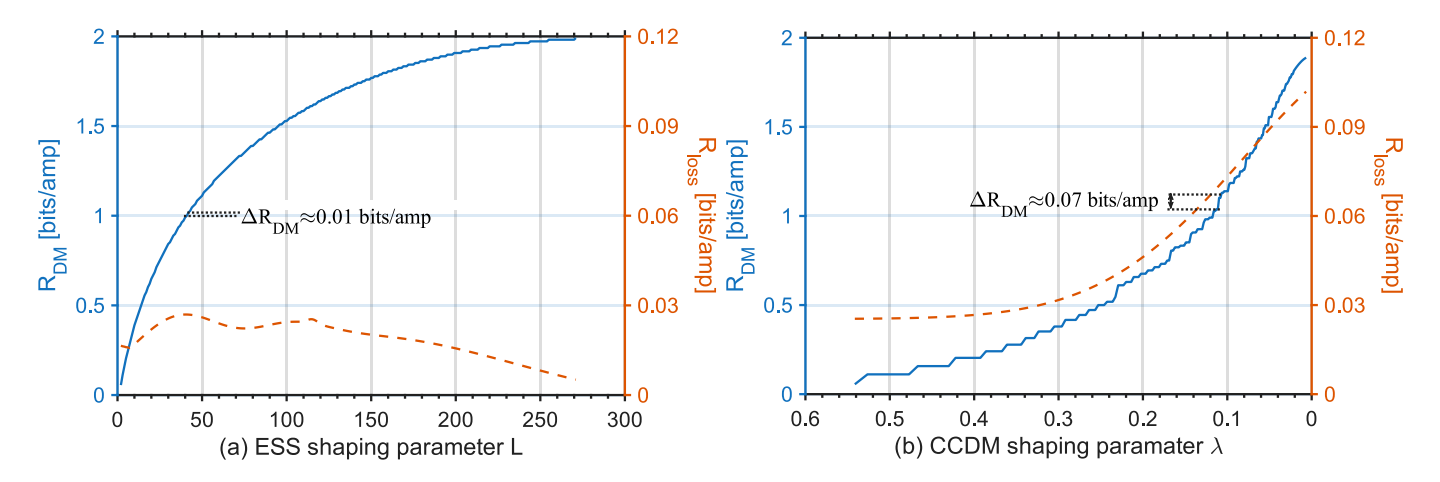


Fig. 3. Comparison of net bit rate $R_{\rm DM}$ and rate loss $R_{\rm loss}$ per distribution matcher (DM) for ESS and CCDM under a fixed block length n=108. (a) Variation of $R_{\rm DM}$ with ESS shaping parameter L from Eq. 14. (b) Variation of $R_{\rm DM}$ with CCDM shaping parameter λ from Eq. 11. The A-PCS scheme based on ESS exhibits finer rate-regulation granularity and lower rate loss compared to CCDM.

When $h > A_0 h_l$, R_{inst} is fixed at $R_{\text{tot-4D}}^{\text{max}}$, which is 10 bits/4D in our design. Thus, R_{inst} is defined as:

$$R_{\text{inst}} = \begin{cases} R_{\text{tot-4D}}^{\text{max}}, & h > A_0 h_1\\ \text{GMI}_{\text{4D}}(\gamma_{\text{FSO}}(h)), & \frac{A_0 h_1}{\gamma_{\text{R}}} \le h \le A_0 h_1\\ 0, & h < \frac{A_0 h_1}{\gamma_{\text{R}}} \end{cases}$$
(29)

Consequently, the ergodic capacity $C_{\rm erg}$ can be mathematically expressed as:

$$C_{\text{erg}} = \int_{\frac{A_0 h_1}{\gamma_{\text{R}}}}^{A_0 h_1} \text{GMI}_{\text{4D}}(\gamma_{\text{FSO}}(h)) f(h) dh + \int_{A_0 h_1}^{\infty} R_{\text{tot-4D}}^{\text{max}} f(h) dh.$$
(30)

This integral can be computed numerically.

B. A-PCS Performance Assessment

ESS adjusts the maximum energy level via the shaping parameter L in Eq. 14, thereby modifying the total number of valid sequences and tuning the net bit rate $R_{\rm DM}$. In contrast, CCDM directly generates amplitude sequences matching a target probability distribution via arithmetic coding [27], allowing adjustment of $R_{\rm DM}$ through the shaping parameter λ in Eq. 11. As shown in Fig. 3, ESS achieves quasi-continuous control over $R_{\rm DM}$ by varying L from 2 to 271. The resulting rate granularity $\Delta R_{\rm DM}$ is approximately 0.01 bits/amplitude, covering a range from 0.05 to 1.98 bits/amplitude. Throughout this range, the rate loss R_{loss} remains below 0.027 bits/amplitude, with a minimum of 0.005 bits/amplitude. In comparison, CCDM-with λ varying from 0.006 to 0.54-exhibits a coarser granularity of $\Delta R_{\rm DM} \approx$ 0.05-0.07 bits/amplitude, which is about seven times larger than that of ESS. The achievable rate range for CCDM is 0.05-1.88 bits/amplitude, slightly narrower than ESS. Moreover, as λ increases, the rate loss of CCDM grows exponentially, reaching up to 0.1 bits/amplitude when $R_{\rm DM}$ lies between $1\sim2$ bits/amplitude. Such high rate loss severely constrains the achievable capacity.

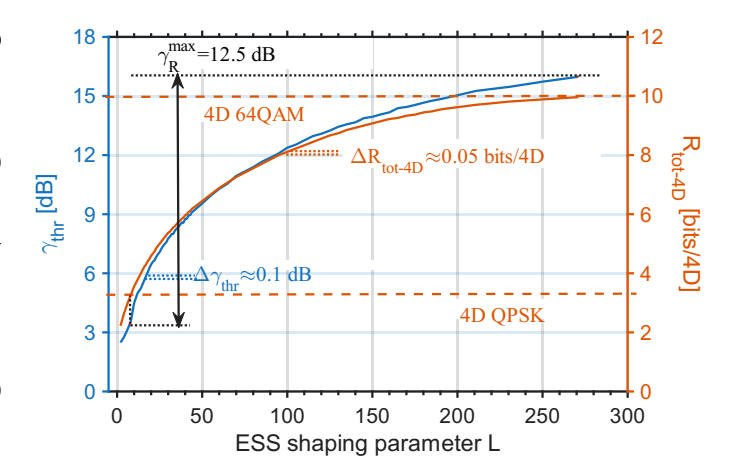


Fig. 4. Performance of A-PCS based on ESS with fixed block length n=108 and FEC rate $R_{\rm C}=5/6$. Left: Post-FEC error-free transmission SNR threshold $\gamma_{\rm thr}$ versus ESS shaping parameter L. Right: Total net bit rate of 4D PCS-64QAM $R_{\rm tot-4D}$ versus L. Orange dashed lines indicate $R_{\rm tot-4D}$ for conventional 4D-64QAM and 4D-QPSK. ESS-based A-PCS demonstrates wide dynamic range and fine granularity in rate adaptation.

For each value of $R_{\rm DM}$ in Fig. 3, the corresponding total net bit rate $R_{\text{tot-4D}}$ is computed via Eq. 23. We maintain a fixed block length n=108 and an FEC rate of 5/6. Under the sign-amplitude separation architecture shown in Fig. 2, $R_{\rm DM}$ ranges from 2 to 10. The maximum $R_{\rm tot-4D}$ equals that of conventional 4D-64QAM, while the minimum falls below that of 4D-QPSK. This occurs because, under strong shaping, PCS-64QAM approaches QPSK behavior: most DM outputs correspond to low-energy amplitudes, yet each requires four amplitude encodings, reducing coding efficiency. Therefore, when $R_{\rm DM}=10/3$, the system switches directly to 4D-QPSK rather than further reducing $R_{\rm DM}$. Consequently, $R_{\rm tot-4D}$ is regulated within the interval $[R_{\rm tot\text{-}4D}^{\rm min}, R_{\rm tot\text{-}4D}^{\rm max}] = [10/3, 10]$ (accounting for FEC overhead), as indicated by orange dashed lines in Fig. 4. Within this range, the post-FEC error-free SNR threshold $\gamma_{\rm thr}$ varies from 3.5 dB to 16 dB, yielding a maximum A-PCS control range $\gamma_{\rm R}^{\rm max}=12.5$ dB. The corresponding rate control granularity $\Delta R_{\text{tot-4D}}$ is about 0.05

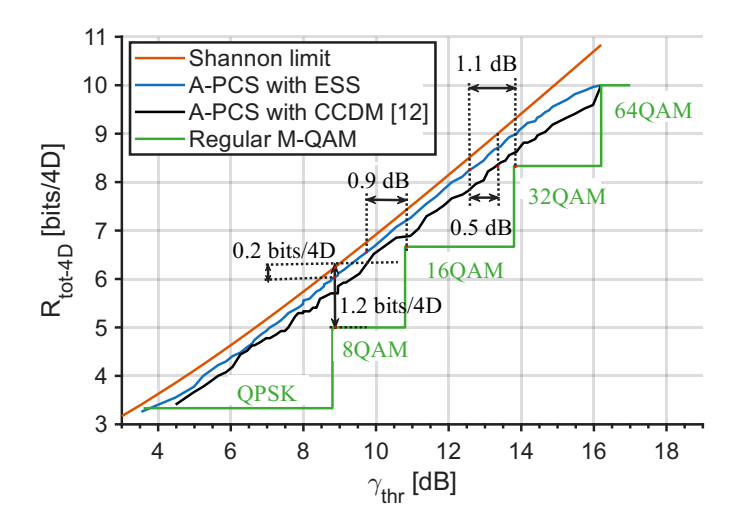


Fig. 5. Simulation of A-PCS based on ESS/CCDM with a fixed block length n=108 and $R_{\rm C}=\frac{5}{6}$, the capacity of Shannon limit and bit rate adaptation based on conventional M-QAM are also presented as baseline. Post-FEC errorfree transmission SNR threshold $\gamma_{\rm thr}$ versus total net bit rate $R_{\rm tot-4D}$. A-PCS based on ESS shows a smoother regulation and higher net bit rate than A-PCS based on CCDM over the entire range, and a much higher spectral efficiency than that of conventional M-QAM. The relationship between $\gamma_{\rm thr}$ and $R_{\rm tot-4D}$ can be stored as a lookup table (LUT) for A-PCS control.

bit/4D-symbol, and the SNR control accuracy $\Delta\gamma_{\rm thr}$ is 0.1 dB. These results confirm that ESS-based A-PCS enables quasicontinuous rate adaptation, closely approaching the theoretical capacity limit.

Fig. 5 compares A-PCS using ESS and CCDM, alongside conventional M-QAM adaptive schemes and the Shannon limit. Conventional M-QAM adaptation employs five discrete modulation formats (QPSK, 8QAM, 16QAM, 32QAM, 64QAM), leading to significant gaps in both rate and SNR adaptation and suboptimal spectral efficiency. In contrast, ESSbased A-PCS offers two key advantages: (1) near-continuous rate and SNR control granularity improves spectrum utilization; (2) low rate loss and energy optimization via the Maxwell-Boltzmann distribution provide substantial shaping gains. Specifically, the gap to the Shannon limit is only about 0.2 bit/4D-symbol-significantly smaller than the 1.2 bit/4Dsymbol gap of conventional 8QAM. Compared to uniform 16QAM, a shaping gain of 0.9 dB is achieved; this is 1.1 dB higher than uniform 32QAM and 0.5 dB superior to CCDM-based A-PCS, owing to lower rate loss. These results underscore the wide dynamic range, high spectral efficiency, and fine adaptation granularity of ESS-based A-PCS. The mapping between $\gamma_{\rm thr}$ and $R_{\rm tot-4D}$ can be stored as a lookup table for real-time adaptive control.

IV. SIMULATION RESULTS UNDER FSO CHANNEL WITH TURBULENCE AND POINTING ERRORS

In this section, we evaluate the performance of the A-PCS system over an FSO channel impaired by turbulence and pointing errors. The turbulence severity is characterized by the Rytov variance $\sigma_{\rm R}^2$, as defined in Eq. 7. Similarly, the pointing error severity is quantified by the standard deviation of the pointing error displacement $\sigma_{\rm s}$ at the receiver, provided in Eq. 9. Based on Table I and references [6], [15], we consider

TABLE I FSO SYSTEM CONFIGURATION

FSO link	
Parameter	Value
Wavelength(λ)	1550 nm
Efficiency of O/E conversion (κ)	1
Tx-Rx Link distance (L)	3 km
Attenuation	0.2 dB/km
Receiver radius (a)	5 cm
Corresponding Beam radius at 3 km (w_z)	$\cong 2.1 \text{ m}$
Rytov Variance $(\sigma_{\rm R}^2)$	0.07-1.55
Corresponding jitter standard deviation(σ_s)	0.01-0.6 m

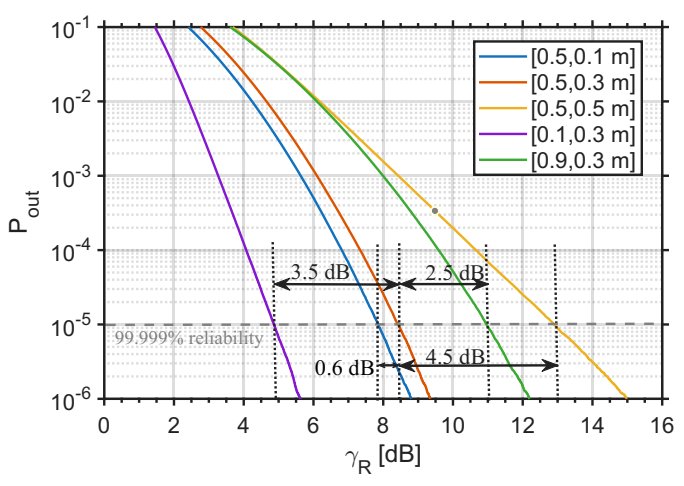


Fig. 6. A-PCS control range $\gamma_{\rm R}$ versus outage probability $P_{\rm out}$ with five different pairs of $[\sigma_{\rm R}^2,\sigma_{\rm s}]$ which is indicated in legend. The outage probability of 10^{-5} , which represents a reliability of 99.999%, is shown as a gray dashed line as a baseline. An increase in pointing errors will rapidly increase the outage probability.

a point-to-point link with a span of 3 km. The transmitter operates at a wavelength of $\lambda=1550$ nm. The receiver is equipped with an aperture radius of a=5 cm and an O/E conversion efficiency of $\kappa=1$. For the channel parameters, we assume an attenuation of 0.2 dB/km under clear air conditions, resulting in a path loss coefficient of $h_l=0.73$. Regarding impairment parameters, $\sigma_{\rm s}$ ranges from 0.01 (low pointing errors) to 0.6 (high pointing errors), while $\sigma_{\rm R}^2$ varies between 0.07 (weak turbulence) and 1.55 (strong turbulence).

Figure 6 presents the variation of outage probability with respect to the control range for five distinct combinations of $\sigma_{\rm s}$ and $\sigma_{\rm R}^2$. The outage probability level of 10^{-5} , which corresponds to a reliability of 99.999%, is depicted as a gray dashed line serving as a baseline. In the first scenario, $\sigma_{\rm R}^2$ is fixed at 0.5, while $\sigma_{\rm s}$ is set to 0.1 m, 0.3 m, and 0.5 m. As the pointing error increases, the minimum control range required to achieve the target outage probability of 10^{-5} rises. Specifically, for $\sigma_s = 0.1 \,\mathrm{m}$, a control range of $7.9\,\mathrm{dB}$ is necessary. For $\sigma_\mathrm{s}=0.3\,\mathrm{m}$, the requirement increases to 8.5 dB, representing an increment of 0.5 dB compared to the $0.1\,\mathrm{m}$ case. When σ_{s} is increased to $0.5\,\mathrm{m}$, the transmission quality degrades significantly, necessitating an additional control range of 4.5 dB to 13 dB to maintain the same reliability. In the second scenario, σ_s is fixed at 0.3 m, and $\sigma_{\rm R}^2$ is varied as 0.1, 0.5, and 0.9. The corresponding

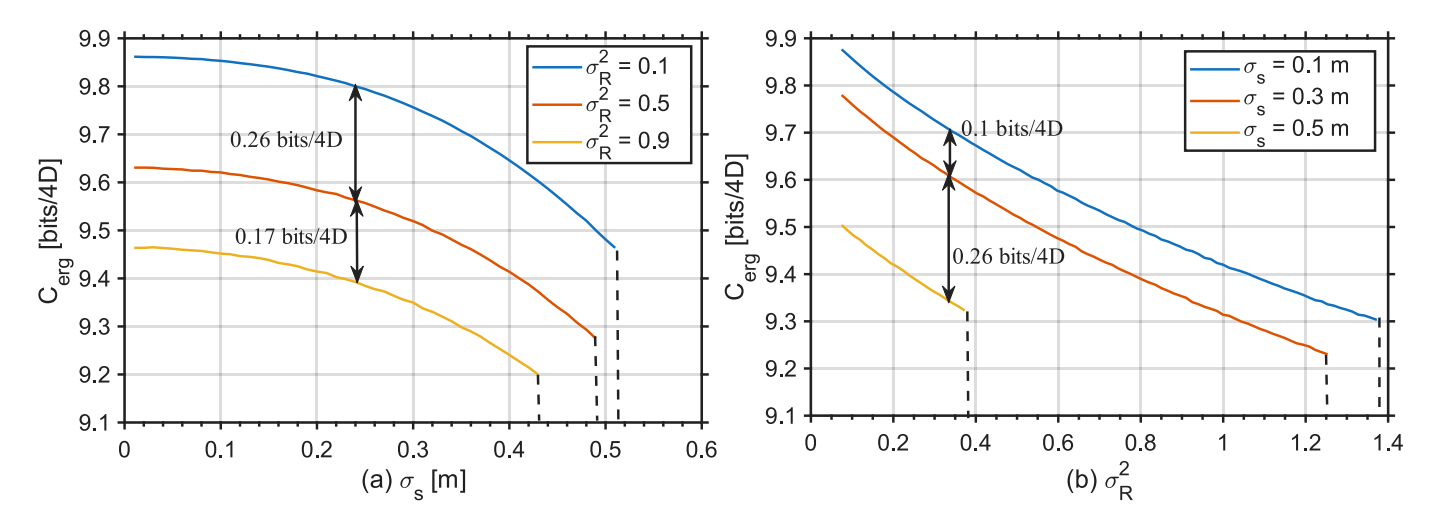


Fig. 7. Performance of ergodic capacity $C_{\rm erg}$ in different pairs of $[\sigma_{\rm R}^2, \sigma_{\rm s}]$ with control range $\gamma_{\rm R}$ is set to 12.5 dB as shown in Fig. 5. $C_{\rm erg}$ will be null when $P_{\rm out}$ is greater than 10^{-5} . Increasing $\sigma_{\rm s}$ and $\sigma_{\rm R}^2$ will lead to a continuous decrease in $C_{\rm erg}$.

control range requirements are: $5\,\mathrm{dB}$ for $\sigma_\mathrm{R}^2=0.1,~8.5\,\mathrm{dB}$ for $\sigma_\mathrm{R}^2=0.5$ (indicating a degradation of $3.5\,\mathrm{dB}$), and an additional $2.5\,\mathrm{dB}$ to $11\,\mathrm{dB}$ for $\sigma_\mathrm{R}^2=0.9$, resulting in a total range of up to $11\,\mathrm{dB}$. This behavior can be explained by the Rayleigh distribution of the pointing error. An increase in σ_s simultaneously amplifies the variance in both elevation and horizontal dimensions, leading to a rapid deterioration in transmission performance. For the A-PCS system, which has a maximum control range of $12.5\,\mathrm{dB}$, the target reliability is unattainable for the parameter set $[\sigma_\mathrm{R}^2,\sigma_\mathrm{s}]=[0.9,0.3\,\mathrm{m}].$

To further evaluate the control performance, we employ the ergodic capacity $C_{\rm erg}$, as defined in Eq. 30, which characterizes the average spectral efficiency of the A-PCS system. The analysis is based on Fig. 7, where we fix either $\sigma_{\rm R}^2$ or $\sigma_{\rm s}$ while varying the other parameter, with the control range γ_R set to its maximum value of 12.5 dB. According to Fig. 5, a transmission interruption is triggered when the control range required to maintain the target outage probability (10^{-5}) exceeds 12.5 dB. In the left sub-figure of Fig. 7, an increase in σ_s intensifies the instantaneous attenuation, leading to a monotonic decrease in C_{erg} . For example, when $\sigma_{\text{R}}^2 = 0.5$, C_{erg} degrades steadily by 0.26 bits/4D relative to the case with $\sigma_{\rm R}^2=0.1$. A further increase in $\sigma_{\rm R}^2$ to 0.9 causes an additional degradation of 0.17 bits/4D, and $C_{\rm erg}$ continues to decline until the transmission interruption point. In the right sub-figure, $C_{\rm erg}$ decreases as $\gamma_{\rm R}$ increases. The case with $\sigma_{\rm s}=0.3$ demonstrates greater stability than $\sigma_{\rm s}=0.1$, exhibiting a deterioration of 0.1 bits/4D. When σ_s is increased to 0.5, the degradation extends by 0.26 bits/4D. Notably, at the transmission interruption point, $C_{\rm erg}$ attains its maximum value for $\sigma_s = 0.5$. This analysis reveals that although elevated $\sigma_{\rm s}$ values lead to consistently low $C_{\rm erg}$, the associated instantaneous decay fluctuations become excessively violent, resulting in a high incidence of out-of-control decays. As a consequence, the target interruption probability cannot be maintained before C_{erg} drops to a critically low level.

Finally, in Fig. 8, we present the ergodic capacity $C_{\rm erg}$ as a function of $\sigma_{\rm s}$ and $\gamma_{\rm R}$ for a target outage probability. Adaptive

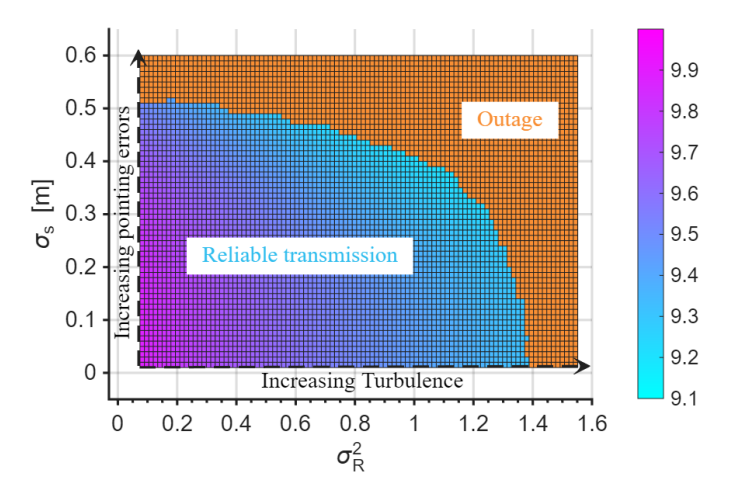


Fig. 8. Performance of ergodic capacity $C_{\rm erg}$ in different pairs of $[\sigma_{\rm R}^2,\sigma_{\rm s}]$ with control range $\gamma_{\rm R}$ is set to 12.5 dB. The heatmap depicts the value and trend of $C_{\rm erg}$, with the color bar on the right indicating the scale. The proposed A-PCS system can maintain reliable transmission and high spectral efficiency over a wide range of channel variations.

control is applied over the full A-PCS range of 12.5 dB. Transmission is deemed reliable if the outage probability is below 10^{-5} ; otherwise, it is classified as an outage. For each pair of $\sigma_{\rm s}$ between 0.01 m to 0.6 m and $\gamma_{\rm R}$ between 0.07 to 1.55 satisfying the reliable transmission criterion, a heatmap depicts the value and trend of C_{erg} , with the color bar on the right indicating the scale. We observe that as $\sigma_{\rm s}$ increases, $C_{\rm erg}$ initially remains high, but when $\sigma_{\rm s}$ exceeds 0.4 m, performance degrades rapidly, culminating in outage at $\sigma_{\rm s}=0.51$ m. In contrast, increasing $\gamma_{\rm R}$ results in a steady decline in C_{erg} , with reliable transmission sustained up to $\gamma_{\rm R}=1.39.$ The graph indicates that along the horizontal axis (varying $\gamma_{\rm R}$), $C_{\rm erg}$ reaches lower values, meaning that higher γ_R introduces greater instantaneous attenuation, but the attenuation depth increases gradually. Conversely, along the vertical axis (varying σ_s), outage occurs at higher C_{erg} values, implying that increasing $\sigma_{\rm s}$ rapidly elevates the probability of deep attenuation, thus hindering the system's ability to maintain the target outage probability.

V. DISCUSSION AND CONCLUSION

We propose a comprehensive ESS-based A-PCS architecture, which explicitly accounts for the rate loss incurred by finite-length distributed matching in practical deployments. For FSO channels under specific atmospheric conditions—including turbulence, pointing errors, and path loss-we derive analytical expressions for transmission reliability and ergodic capacity subject to a target outage probability. Numerical results demonstrate that our scheme achieves a transmission reliability of 99.999% even under strong turbulence and significant misalignment, while offering finer control granularity and improved spectral efficiency over existing approaches. Future research will focus on extending the operational range to more challenging channel conditions, developing analytical frameworks for reliability and capacity under non-ideal CSI feedback, and conducting experimental validation of the proposed framework.

ACKNOWLEDGMENTS

This work was supported by the Natural Science Basic Research Program of Shaanxi Department of Science and Technology (2023-JC-JQ-58).

REFERENCES

- I. F. Akyildiz, C. Han, Z. Hu, S. Nie, and J. M. Jornet, "Terahertz band communication: An old problem revisited and research directions for the next decade," *IEEE Transactions on Communications*, vol. 70, no. 6, pp. 4250–4285, 2022.
- [2] S. Nie and I. F. Akyildiz, "Channel modeling and analysis of inter-small-satellite links in terahertz band space networks," *IEEE Transactions on Communications*, vol. 69, no. 12, pp. 8585–8599, 2021.
- [3] C. Han, W. Gao, Z. Yin, C. Yang, M. Peng, and W. Zhang, "Joint Communication and Radar Sensing for Terahertz Space-Air-Ground Integrated Networks (SAGIN)," arXiv preprint arXiv:2502.17811, 2025.
- [4] V. Dhasarathan, M. Singh, and J. Malhotra, "Development of high-speed FSO transmission link for the implementation of 5G and Internet of Things," Wireless Networks, vol. 26, no. 4, pp. 2403–2412, 2020.
- [5] M. A. Khalighi and M. Uysal, "Survey on free space optical communication: A communication theory perspective," *IEEE communications surveys & tutorials*, vol. 16, no. 4, pp. 2231–2258, 2014.
 [6] A. A. Farid and S. Hranilovic, "Outage capacity optimization for
- [6] A. A. Farid and S. Hranilovic, "Outage capacity optimization for free-space optical links with pointing errors," *Journal of Lightwave technology*, vol. 25, no. 7, pp. 1702–1710, 2007.
- [7] A. Prokes, "Atmospheric effects on availability of free space optics systems," *Optical engineering*, vol. 48, no. 6, pp. 066 001–066 001, 2009.
- [8] V. V. Mai and A. T. Pham, "Adaptive multi-rate designs for hybrid FSO/RF systems over fading channels," in 2014 IEEE Globecom Workshops (GC Wkshps). IEEE, 2014, pp. 469–474.
- [9] X. Wang, H. Li, and Q. Wu, "Optimizing adaptive coding and modulation for satellite network with ML-based CSI prediction," in 2019 IEEE Wireless Communications and Networking Conference (WCNC). IEEE, 2019, pp. 1–6.
- [10] F. R. Kschischang et al., "Optimal nonuniform signaling for Gaussian channels," *IEEE Transactions on Information Theory*, vol. 39, no. 3, pp. 913–929, 1993.
- [11] A. Elzanaty and M.-S. Alouini, "Adaptive coded modulation for IM/DD free-space optical backhauling: A probabilistic shaping approach," *IEEE Transactions on Communications*, vol. 68, no. 10, pp. 6388–6402, 2020.
- [12] F. P. Guiomar, A. Lorences-Riesgo, D. Ranzal, F. Rocco, A. N. Sousa, M. A. Fernandes, B. T. Brandão, A. Carena, A. L. Teixeira, M. C. Medeiros et al., "Adaptive probabilistic shaped modulation for high-capacity free-space optical links," *Journal of Lightwave Technology*, vol. 38, no. 23, pp. 6529–6541, 2020.

- [13] B. T. Brandao, M. A. Fernandes, P. A. Loureiro, F. P. Guiomar, and P. P. Monteiro, "Cooperative FSO and mmWave system for reliable 200G wireless transmission," *IEEE Photonics Technology Letters*, vol. 34, no. 24, pp. 1333–1336, 2022.
- [14] X. Zhu and J. M. Kahn, "Free-space optical communication through atmospheric turbulence channels," *IEEE Transactions on communications*, vol. 50, no. 8, pp. 1293–1300, 2002.
- [15] W. Aman, M. Qaraqe, M. M. U. Rahman, S. Al-Kuwari, and T. Y. Al-Naffouri, "Effective Capacity Analysis for Hybrid FSO/THz Backhaul Link in 6G Networks," *IEEE Wireless Communications Letters*, 2025.
- [16] I. I. Kim, B. McArthur, and E. J. Korevaar, "Comparison of laser beam propagation at 785 nm and 1550 nm in fog and haze for optical wireless communications," in *Optical wireless communications III*, vol. 4214. Spie, 2001, pp. 26–37.
- [17] L. C. Andrews, R. L. Phillips, C. Y. Hopen, and M. Al-Habash, "Theory of optical scintillation," *Journal of the Optical Society of America A*, vol. 16, no. 6, pp. 1417–1429, 1999.
- [18] M. Al-Habash, L. C. Andrews, and R. L. Phillips, "Mathematical model for the irradiance probability density function of a laser beam propagating through turbulent media," *Optical engineering*, vol. 40, no. 8, pp. 1554–1562, 2001.
- [19] N. D. Chatzidiamantis, H. G. Sandalidis, G. K. Karagiannidis, S. A. Kotsopoulos, and M. Matthaiou, "New results on turbulence modeling for free-space optical systems," in 2010 17th International Conference on Telecommunications. IEEE, 2010, pp. 487–492.
- [20] H. Samimi, "Distribution of the sum of K-distributed random variables and applications in free-space optical communications," *IET optoelectronics*, vol. 6, no. 1, pp. 1–6, 2012.
- [21] H. Kaushal, V. Jain, and S. Kar, "Free-space optical channel models," in *Free space optical communication*. Springer, 2017, pp. 41–89.
- [22] L. C. Andrews, R. L. Phillips, and C. Y. Hopen, Laser beam scintillation with applications. SPIE press, 2001, vol. 99.
- [23] F. Davidson, C. J. Juan, and A. R. Hammons, "Channel fade modeling for free-space optical links," in 2010-MILCOM 2010 MILITARY COM-MUNICATIONS CONFERENCE. IEEE, 2010, pp. 802–807.
- [24] A. Jurado-Navas, J. M. Garrido-Balsellss, M. Castillo-Vázquez, and A. Puerta-Notario, "A computationally efficient numerical simulation for generating atmospheric optical scintillations," in *Numerical Simulations* of *Physical and Engineering Processes*. InTech, 2011, pp. 157–180.
- [25] D. Bykhovsky, "Simple generation of gamma, gamma-gamma, and K distributions with exponential autocorrelation function," *Journal of Lightwave Technology*, vol. 34, no. 9, pp. 2106–2110, 2016.
- [26] S. Arnon, "Effects of atmospheric turbulence and building sway on optical wireless-communication systems," *Optics letters*, vol. 28, no. 2, pp. 129–131, 2003.
- [27] P. Schulte and G. Böcherer, "Constant composition distribution matching," *IEEE Transactions on Information Theory*, vol. 62, no. 1, pp. 430–434, 2015.
- [28] A. Amari, S. Goossens, Y. C. Gültekin, O. Vassilieva, I. Kim, T. Ikeuchi, C. M. Okonkwo, F. M. Willems, and A. Alvarado, "Introducing enumerative sphere shaping for optical communication systems with short blocklengths," *Journal of Lightwave Technology*, vol. 37, no. 23, pp. 5926–5936, 2019.
- [29] Y. C. Gültekin, W. J. van Houtum, A. G. C. Koppelaar, F. M. J. Willems, and W. J. van Houtum, "Enumerative Sphere Shaping for Wireless Communications With Short Packets," *IEEE Transactions on Wireless Communications*, vol. 19, no. 2, pp. 1098–1112, 2020.
- [30] G. Böcherer, "Achievable rates for probabilistic shaping," arXiv preprint arXiv:1707.01134, 2017.
- [31] J. Cho, L. Schmalen, and P. J. Winzer, "Normalized generalized mutual information as a forward error correction threshold for probabilistically shaped QAM," in 2017 European Conference on Optical Communication (ECOC). IEEE, 2017, pp. 1–3.
- [32] T. Fehenberger, D. S. Millar, T. Koike-Akino, K. Kojima, and K. Parsons, "Multiset-Partition Distribution Matching," *IEEE Transactions on Communications*, vol. 67, no. 3, pp. 1885–1893, 2019.